MAX-PLANCK-INSTITUT FÜR PLASMAPHYSIK

GARCHING BEI MÜNCHEN

Report on First Results of ASDEX Upgrade Operation with the LYRA Divertor

ASDEX Upgrade team
(compiled by J. Neuhauser)

IPP 1/311 September 1997

Die nachstehende Arbeit wurde im Rahmen des Vertrages zwischen dem Max-Planck-Institut für Plasmaphysik und der Europäischen Atomgemeinschaft über die Zusammenarbeit auf dem Gebiete der Plasmaphysik durchgeführt.

Abstract:

Preliminary results of the first two months of ASDEX Upgrade operation with the new Lyra divertor (DV-II) are presented and compared to those obtained with the previous divertor configuration (DV-I). Emphasis is placed on issues which, according to common knowledge, might be related to the edge / divertor goemetry, in particular upper density limits, H mode characteristics, particle control and impurity behaviour. The experimental facts are complemented by B2-Eirene modelling results. Remarkable changes in core MHD behaviour are also included, but their origin is not yet clear.

IPP 1 / 311 September 1997

Report on First Results of ASDEX Upgrade Operation with the LYRA Divertor

ASDEX Upgrade team
(compiled by J. Neuhauser)

Max-Planck-Institut für Plasmaphysik
Garching, Germany, EURATOM Association

1. Introduction

In a first phase ASDEX Upgrade has been operated for approximately 2 months with the new Lyra (DV-II) divertor configuration. Fig.1 shows a comparison of the previous DV-I configuration (see e.g. IAEA review paper /1/) and the new Lyra divertor /2/. One important goal of this campaign was to provide information on the dependence of density limits on divertor geometry, to support a decision on the installation of the gas-box divertor MkII-GB in JET. The present report describes results of this campaign with emphasis on this specific purpose. As one major edge diagnostics (Lithium beam density measurements) was not operational, and the detailed analysis of the results has just started, the findings presented here have to be considered preliminary. Some evident conclusions from the comparison between the more closed DV-II and the more open DV-I configuration are, however: (1) no major changes in a typical high power density ramp-up scenario (Fig.2) including similar values of the ultimate L-mode density limit, (2) a significant change in the divertor neutral density behaviour during density ramp-up, (3) a strong improvement of the helium pumping capability (where now, in H-modes, ratios of helium removal to energy confinement times $\tau^*_{He}/\tau_E \approx 4$ have been actually reached). Further changes were observed also in the MHD activity and in the L-H power transition threshold, but it is as yet unclear, whether these are directly linked to the divertor modifications.

The campaign comprised 400 plasma discharges in single null configuration, with the standard orientation of the toroidal field (ion grad-B drift towards divertor). Operating parameters were in the range $B_t \leq 3.0$T, $I_p \leq 0.8$MA; $P_{NI} \leq 10$ MW, $P_{ICRH} \leq 3$ MW, $P_{ECRH} \leq 0.5$ MW. The plasma equilibria used have low triangularity and maintain a similar distance to the antenna limiters as before. Both D^+ and (to a lesser extent) H^+ were used as background plasmas and beam injected species and the vessel was repeatedly boronized. Pellets were injected with a centrifuge from the low and high field side (though these results

will not be reported here). Impurity puffing with N, Ne, Ar and He was carried out. The available 14 turbo-pumps were used to pump during the discharge as before. The new cryo-pumps were successfully tested, but not yet used during discharges. The main chamber wall elements (protective limiters etc.) were unchanged from previous campaigns. Fig. 3 shows again the geometry of DV-II, and gives also the nominal values for the bypass conductances and for the pumping efficiencies.

Though, after an initial conditioning and learning phase, the machine performance has reached a stationary level of overall plasma performance (in terms of confinement quality, operational limits, etc.), a firm comparison must await detailed data analysis and further explorations of the available parameter and configuration space. Some new or reconstructed edge and divertor diagnostics were not yet fully operational or calibrated and the magnetic equilibrium reconstruction needs further confirmation. The following, preliminary and partly qualitative statements refer to the machine status as achieved in July / August 1997.

2. Density Limits

2.1. Ohmic and L-mode density limit

The Ohmic and L-mode density limits were explored using, as far as possible, the same experimental scenarios and definitions as before. Essentially the same global density limits can be obtained with the Lyra divertor as with DV-I, and the same basic physical phenomena (e.g. Marfe evolution) are observed (Fig.4). The Greenwald limit can be reached or slightly exceeded with gas puffing. The L-mode density limit is sensitive to the quality of the wall boronization. The limit decreases weakly with increased antenna-plasma distance in the mid plane, but is rather insensitive to the location of the gas puff (main chamber vs. divertor). A significant increase of density beyond the Greenwald limit was again obtained with pellet injection.

Divertor detachment appears to occur at comparable line-averaged densities (see also the paragraph on CDH-mode below). A more exact comparison and a quantitative assessment in terms of local parameters will require however further detailed work, as the divertor diagnostic suite for the Lyra is necessarily rather different from the previous one. For example, the C_{III} radiation cord integral previously used as a detachment monitor is not identically available. The maximum divertor neutral pressure immediately before the disruption seems to be significantly higher with the Lyra.

2.2. H-modes at high density

The maximum achievable density in H-mode (determined by back transition to L-mode) with the Lyra configuration is slightly below the Greenwald limit, as it was with DV-I (Fig.4) and the global time history of a typical H-mode density limit discharge is also similar (Fig.2). Again, the stored plasma energy is found to decrease with increasing density. However, in contrast to the L-mode density limit the H-mode limit (H->L mode transition) is not sensitive to the quality of wall boronization.

3. H-Mode Characteristics

3.1. H-Mode power threshold

For the limited number of deuterium discharges adequate for power threshold analyses, the power threshold in DV-II shows a tendency to be higher than in DV-I by about 15%, as shown in Fig.5. This effect in terms of gross input power is moderate but clear. The net power through the separatrix requires correction for the radiation power inside the separatrix, which is not reliably available for these discharges. These data points were taken at the end of the first experimental period with DV-II after a boronization such that radiation losses and hydrogen concentration were as low as possible. They are therefore believed to be taken under plasma conditions comparable to those from DV-I. For the very limited number of discharges performed in hydrogen, a similar result is obtained, suggesting that the hydrogen concentration is not the reason, but cannot be excluded within the present experimental uncertainties.
The reason for the increase may be due to a lack of conditioning of the tokamak wall and target plates or / and to the properties of DV-II. The carbon flux from the protection limiters is somewhat higher in DV-II than in DV-I (see section below) and this may also be a reason for the higher power threshold. The increase of this carbon influx during the discharge is probably the reason for the weaker power hysteresis of the H to L transition observed in DV-II. These points are expected to be clarified during the next experimental campaign

3.2. ELM properties

The behaviour of Edge Localised Modes (ELMs) is found very similar in the DV-I and DV-II phases of ASDEX Upgrade. With both divertor geometries, type I and type III ELMs are found. In addition, compound ELMs and "mixed ELMs" (i.e. a train of type III ELMs following a large type I ELM) are found at high levels of gas puffing and after

sudden reduction of heating power, respectively. The effect of ELMs transport in both divertor geometries can be characterised by a comparison of ELM frequency, energy loss and particle loss per ELM from the main plasma. These parameters can be compared for a pair of discharges with DV-I (#7954) and DV-II (#9349) and otherwise similar plasma parameters (Single Null geometry with ion- grad B drift towards X-point (favourable direction), plasma current I_p= 0.8 MA, auxiliary heating by deuterium neutral beam injection into a deuterium plasma, P_{NBI} = 5 MW, toroidal field B_t = 2.1 T). It is found that under these conditions the line averaged density (at closed gas valve) adjusts itself to the practically identical value $\bar{n}_e = 5.7 \times 10^{19} m^{-3}$ in both configurations.

The plasma shape for DV-II discharges is modified to facilitate separatrix passage through the divertor throat and to optimise the strike point localisation. This results in a 10% higher triangularity of the DV-II plasma (δ = 0.103) compared to the DV-I plasma (δ = 0.094). The discharge #9349 has higher stored energy (W_{MHD} = 500 kJ) than the comparison discharge #7954 (W_{MHD} = 420 kJ). Fig.6 shows time traces for short phases of both discharges: The time between the onset of subsequent ELMs (ELM period), the relative energy loss $\Delta W/W$ per ELM the particle (electron) loss ΔN per ELM, and the D_α traces measured in the outer divertor.

The ELM frequency for similar plasma parameters and similar radiated power seems somewhat reduced for DV-II as compared to DV-I, which might, however, be due to the changed triangularity. The measurements of particle loss (from central interferometer chord) and energy loss (W_{MHD} from equilibrium reconstruction) for individual ELMs exhibit significant scatter. However, the average relative energy loss ($\Delta W/W$ = 1.6 to 2.6 %) and the average particle loss $\Delta N = 2.5 * 10^{19}$ for the two comparison discharges are equal within the scatter.

3.3. Core MHD behaviour

One of the most conspicuous differences between discharges run with similar wave-forms in the present (Lyra) and old (DV-I) configuration concerns the MHD behaviour, which is now characterised by more pronounced sawtooth, fishbone and neoclassical tearing mode activity. At present we see no clear evidence linking these differences to the modifications in the divertor target plate configuration, although the other, concomitant changes were apparently small. Possible candidates for an explanation are the slightly increased plasma triangularity, the slight downward displacement of the magnetic axis (e.g. vis-à-vis the neutral beam injectors) and changes in the power ramp-up scenario, which were necessitated by changes in the poloidal field coil power supplies. An illustrative example is given by the discharge pair in Fig.7, which shows much stronger MHD activity in the new configuration, leading to a much more drastic drop in normalised β after the

transient maximum, a decrease (rather than increase) with time of the plasma density and ultimately a locking of the mode and a stop of global plasma rotation as seen also in the CX spectroscopy channels.

4. Particle balance and Impurity Behaviour

4.1. Pumping of noble gases

As in DV-I, the divertor compression and pumping of noble gases exhibit a pronounced increase with the neutral deuterium flux density in the divertor. The most evident difference to DV-I is the considerable improvement of Helium pumping for H-mode conditions with moderate or high neutral flux levels. Helium removal 1/e times as short as 0.2 s have been measured for H-mode conditions with high neutral flux level, pointing to very long neutral helium retention times in the divertor. The corresponding value of τ_{HE}^* / τ_E is about 4.

Fig.8 compares for both configurations the global helium recycling flux after a short helium puff during ELMy H-mode. The faster decay rate with DV-II points to a much longer (~ factor 4) effective helium retention time, based on a simple particle balance analysis.

Preliminary analysis of neon pumping reveals a moderate degradation of the pumping time: while in DV-I neon pumping was more efficient than helium pumping under most conditions, the opposite is the case in DV-II.

4.2 Hydrogen recycling and behaviour of intrinsic impurities

No dramatic change in the core plasma impurity composition is observed comparing DV-I and II. Carbon is the dominant impurity, followed by boron, fluorine and oxygen. The carbon level seems to be slightly increased for high power or low edge density conditions with DV-II. Low field side limiter erosion in the main chamber by beam ions is known to be one effective source for the core carbon inventory. It depends sensitively on density, plasma position, shape and choice of NBI sources, but no profound and systematic comparison has yet been made between DV-I and -II. Remarkable was the very long conditioning time of the machine in terms of the H/D ratio. A possible reason may be water from the new CFC tiles, which were not baked before installation.

The hydrogen content at the end of the deuterium campaign was still about 20 % (in a state of aged boronization). Fresh boronizations lead only to temporary reductions of the hydrogen content.

The distribution of the neutral gas in the divertor region is substantially changed. Whereas in DV-I the neutral flux density outside the outer strike zone was usually larger than in the private flux region, except for low recycling condition, it is now always higher in the private flux region. The neutral flux there rises also more steeply with increasing main plasma density .

4.3. Impurity seeding and CDH-Mode performance

The typical CDH-mode scenario (characterized by: type-III ELMs, divertor detachment, electron density profile peaking in connection with moderate confinement improvement, reduction of central transport) was established in DV-II using neon injection (so far only in feed-forward mode because of problems with central bolometer chords) and feedback-control of the divertor hydrogen neutral flux at intermediate levels (Fig.9 a and b show two cases with and without pronounced density peaking). A strong reduction of C_{III} emission in the V-shaped divertor target region indicates detachment in the lower part of the divertor (Fig.10).

No evidence for enhanced divertor radiation compared to DV-I has been observed so far in the Lyra divertor, using nitrogen puffing at 4 toroidally distributed divertor positions. As in DV-I, nitrogen appears in the main chamber, and again detachment seems to be caused primarily by main chamber radiation. However, analysis of the total divertor radiation distribution was not yet possible as the divertor bolometers will only be installed during the present shut-down.

5. B2-Eirene modelling of the Lyra-divertor

5.1. Compression of recycling impurities

B2-Eirene has been used to simulate density ramp-up scenarios for DV-I (without changing any of the validated transport parameters in the code) /3/. From these runs, the compression of neon and helium at the position of the pump duct relative to the mid plane density can be derived. Comparing with the experimental results, the model calculations are obviously able to describe qualitatively as well as quantitatively the experimental behaviour: compression of neon and helium (neon is better compressed than helium) increases with higher neutral gas flux density in the divertor. The basic mechanism for the compression is the recycling cycle in the outer scrape-off layer. For ASDEX Upgrade DV-I the existence of a pumping baffle in the outer divertor is quite important for the observed compression. For the Lyra configuration modelling predicts a much better compression of helium (an

enrichment of helium of typically 2 is now observed in the pumping duct location) than for DV-I (enrichment factors for helium between 0.1 and 0.4). The very good compression of neon in the outside tilted DV-I (enrichment of 1 to 6) is reduced to practically the same as the hydrogen compression (enrichment 1 to 1.5), but is still large enough for effective feedback control.

In the Lyra the pumping duct recycling is now concentrated in the dome region close to the separatrix hit point. Due to the higher electron densities there, creation of impurity neutrals at the plate and reionization of colder neutrals from the dome occur at practically the same position. The better compression of helium in the Lyra is then due to the fact that the helium neutral atoms have longer mean free paths than neon and can therefore escape easier from the inclined target plate region into the dome and from there into the pump.

5.2. L-mode density limit

B2-Eirene had previously reproduced well the experimental findings regarding the L-mode density limit in both ASDEX Upgrade DV-I and JET. Apparently different trends with heating power could be reconciled by the detailed modelling. ASDEX Upgrade showed practically a square-root power dependence of the density limit for relatively low net input powers. JET results also show a square-root like power dependence at low net input powers, but a much weaker power dependence at higher net input powers (both experimental and modelling). This was attributed to the change of the neutral collisionality which determines the scaling. The same was predicted for ASDEX Upgrade DV-I only for net input power into the divertor gas target region above 2.5 MW, a regime, which was not yet reached with the ≤ 8 MW input power used in L-mode density limit studies.

For a typical (although not an actual experimental) Lyra equilibrium configuration, B2-Eirene simulations predict for DV-II a much earlier onset of detachment at the separatrix ($2*10^{19} m^{-3}$) than for DV-I ($3.9*10^{19}$ m^{-3}), both for divertor and mid plane gas puff and with reasonable pumping, transport and C-impurity production (physical and chemical sputtering). Accordingly, the scrape-off layer detachment density limit should be reduced from $4.0*10^{19}$ m^{-3} for DV-I to $3.2*10^{19}$ m^{-3} for the Lyra. The predicted earlier detachment of the separatrix region compared to the global detachment in DV-I is due to the geometry of the Lyra, where neutrals get reflected preferentially towards this hot part of the plasma at the separatrix, whereas in DV-I the inner divertor (which is usually the first to detach) was practically orthogonal. The change of divertor profiles due to this change of geometry (with a much earlier cold separatrix for DV-II and a hotter outer scrape-off layer part trying to keep attached much longer with respect to mid plane density) seems to be confirmed by first Langmuir divertor profiles from the Lyra. The influence of the impurity production model

on the detachment limit in the simulation (Marfe limit prior to complete detachment limit ?) and a reliable edge density profile are both necessary to make a final assessment.

6. Summary and preliminary conclusions

A preliminary analysis of the first operational phase with the new Lyra divertor has revealed no significant changes in macroscopic performance parameters attributable to the changed divertor configuration. In particular, the density limit and the confinement times in discharges without strong core MHD activity have remained virtually unchanged. A major change has occurred in the pumping capability for helium which has improved to the point that a ratio of $\tau^*_{He}/\tau_E \approx 4$ has been achieved (previously, values in this range were quoted as results of extrapolation to infinitely fast pumping). This trend for helium was expected and is well in agreement with B2-Eirene modelling calculations, which reproduce also the trends observed with other recycling impurities. The observed invariance of the density limit is in partial disagreement with modelling calculations, which have well explained previous results of ASDEX Upgrade DV-I and JET Mk-I and Mk-IIA, and predict a decrease in maximum separatrix density by 20% in the change-over from DV-I to Lyra. As the separatrix density was not directly measured in this experimental campaign, a possible change in its magnitude cannot be excluded, though there is no indication for such a change from the DCN interferometer. We should mention also that the modelling was not yet done with experimental equilibria which might influence (due to e.g. different wall clearance) the density limit in the code runs.

Changes have been observed in more detailed features of divertor behaviour, but need to await a more complete analysis, and partly also the coming into operation of further diagnostics during the next campaign. Definite changes have also been observed in the core MHD behaviour (sawteeth, fishbones, neoclassical MHD modes), but it is doubtful that these are caused directly by the change in the divertor structures. (Minor changes have been simultaneously made to the triangularity of the plasma and the vertical position of the magnetic axis vis-à-vis the axis of the NBI injectors, and ICRF has been used more extensively during phases of the discharge. Modifications in the power supplies necessitated also some changes in the power ramp-up scenarios.). Again these items require the outcome of further analysis work.

References

/1/ M Kaufmann et al.; 16th IAEA Conf., Montreal 1996, IAEA-F1-CN-64/O1-5

/2/ HS Bosch et al.; Report (proposal) IPP1/281; Garching, September 1994

/3/ R Schneider et al.; J. Nucl. Mater. 241-243 (1997) 701

Figures

Fig.1. Cross section of the Lyra divertor (DV-II; bottom) compared to the original divertor configuration (DV-I; top).

Fig 2. Typical density ramp-up discharges in the old (DV-I) and new divertor (DV-II) configuration leading to density limit disruptions (I_p = 0.8 MA, q_{95} = 4). The new tight divertor requires a smoother ramp-up of the heating power, as seen in the right part of the figure, since the limited power supply capabilities of the poloidal magnetic field coils only allow a slower control of the plasma shape. Due to the significantly changed divertor and diagnostic observation geometries, the D_α and C_{III} traces are not directly comparable. The bottom traces represent a bremsstrahlung chord viewing slightly above the X-point. The elevations shortly before the density limit disruptions correspond to the expansion of the Marfe into the plasma bulk. The vertical dashed lines indicate the H-L back-transition, i.e. the H-mode density limit.

Fig.3. Nominal pumping efficiencies and bypass leaks in the Lyra divertor (DV-II).

Fig.4. Comparison of upper L- and H-mode density limit with DV-II (full symbols) and DV-I (shaded symbols) as function of total heating power. All densities are normalised to Greenwald-limit.

Fig.5. L-H power threshold for DV-I and DV-II. The line represents the usual ASDEX Upgrade threshold with DV-I: $P_{th} = 1.7\ \bar{n}_e \times B_T$ [MW 10^{20} m^{-3} T]. Usual representation in the region of linear density dependence: net heating power at the L-H transition versus product of line-averaged density by magnetic field. Conditions: deuterium plasmas, ion grad-B drift in the favourable direction.

Fig.6. Comparison of ELM parameters for two discharges with DV-I (#7954) and DV-II (#9274) with mostly identical parameters (B_t = 2.1T, I_p = 0.8 MA, P_{NBI} = 5 MW): ELM period (time between two adjacent ELMs), relative energy loss $\Delta W/W$ per ELM, particle loss per ELM and H_α trace.

Fig.7. Comparison of the MHD behaviour with the two divertor configurations. The DV-II case shows, in addition to the neoclassical 3/2 mode also existing in the DV-I case, a large m=2/n=1 mode. The second stage of the beta-drop and the suppression of the density rise coincide with locking of both modes and a suppression of global plasma rotation as observed from CX spectroscopy. The first discharge drops back to L-mode at t ≈ 2.44 s,

the second at t = 2.48 s after the mode locking (ELM-behaviour, radial electric field from charge exchange).

Fig.8. Comparison of the global helium recycling flux after a short helium puff during ELMy H-mode. The faster decay rate with DV-II points to a much longer (~ factor 4) effective helium retention time, based on a simple particle balance analysis. The divertor neutral flux density measured below the passive stabiliser coil is $6*10^{22}$ m^{-2} s^{-1} for both discharges, P_{heat}= 7 MW, $\bar{n}_e$= 10^{20} m^{-3}, # 9293: I_p=0.8 MA, q_{95}=4.3 , # 6138: I_p= 1 MA, q_{95}=4, # 9293 additional pellet fuelling.

Fig.9a. Time traces of a CDH-mode discharge with pronounced density peaking, sawtooth stabilisation and confinement improvement ($f_{H,ITER89p}$= 1.4 ... 1.66). The central particle transport is much slower than in # 9316 (next figure), which does not show pronounced electron density peaking. I_p= 0.8 MA, P_{heat}= 7 MW, $\Gamma_{o,div} = 3*10^{22} m^{-2} s^{-1}$.

Fig.9b. Time traces of a CDH-mode discharge without density peaking. Sawteeth are preserved, central particle transport is fast and confinement is low (due to high divertor neutral flux) $f_{H,ITER89p}$= 1.2, I_p= 0.8 MA, P_{heat}= 7 MW, $\Gamma_{o,div} = 6*10^{22} m^{-2} s^{-1}$.

Fig.10. Viewing lines of the divertor spectrometer and C_{III} profiles along the target plates in the inner and outer divertor during the type-I ELMy and the type-III ELMy-CDH phases of the discharges shown in Fig.9. Profiles shown are time-averaged over several ELM cycles. # 9316 (lower picture) had a higher neutral flux density and no pronounced peaking, the higher strike point position is clearly seen in the C_{III} emission during the type-I ELMy phase. The arrows denote the strike point positions on the target. For both discharges, not all of the total available viewing lines displayed in the upper graph are active. The strong reduction of C_{III} emission during neon cooling indicates detachment in the lower part of the divertor.

DV- I

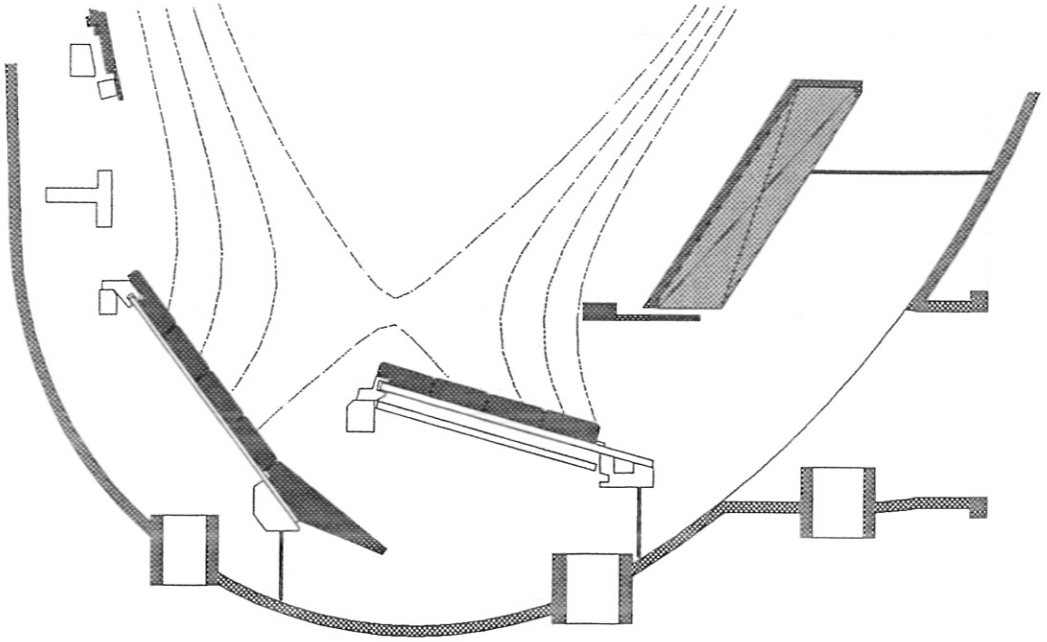

DV- II (LYRA)

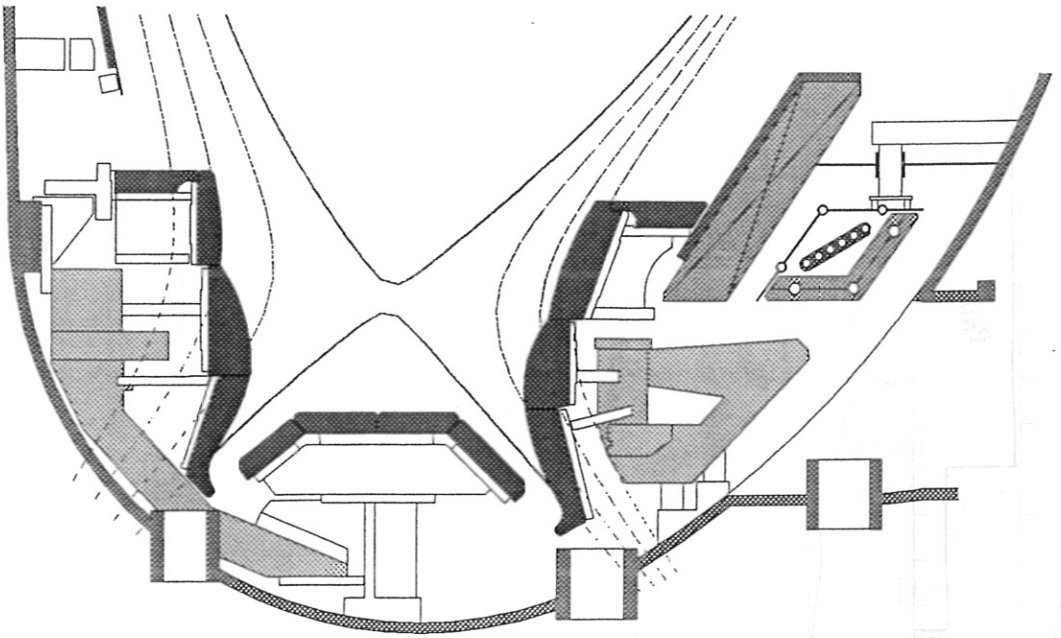

Figure 1

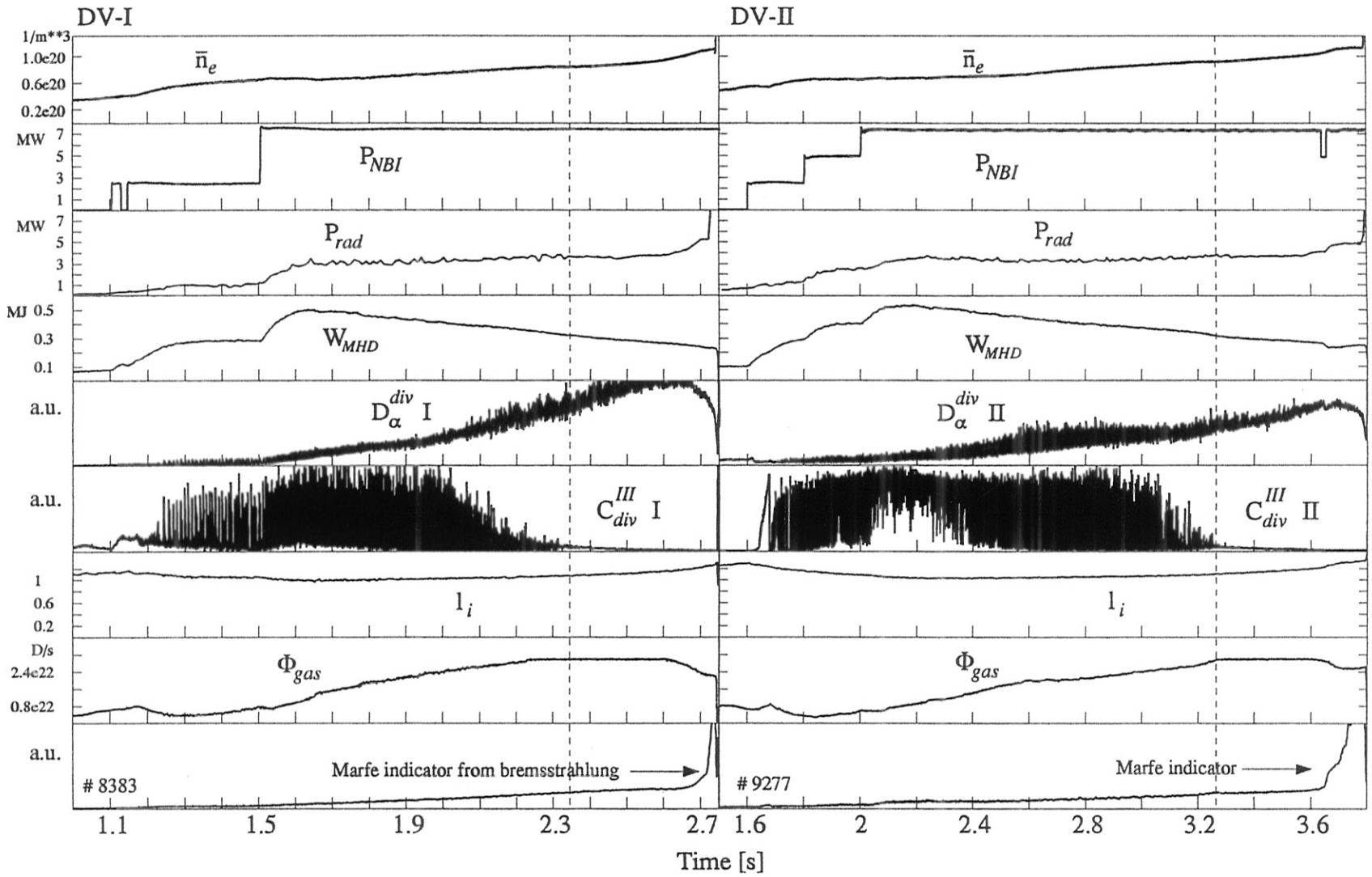
DV-I
DV-II
1/m**3
1.0e20
0.6e20
0.2e20
$\bar{n}_e$
MW
7
5
3
1
P_{NBI}
P_{rad}
MJ
0.5
0.3
0.1
W_{MHD}
a.u.
D_α^{div} I
D_α^{div} II
C_{div}^{III} I
C_{div}^{III} II
1
0.6
0.2
l_i
D/s
2.4e22
0.8e22
Φ_{gas}
Marfe indicator from bremsstrahlung
Marfe indicator
8383
9277
1.1
1.5
1.9
2.3
2.7
1.6
2
2.4
2.8
3.2
3.6
Time [s]

Figure 2

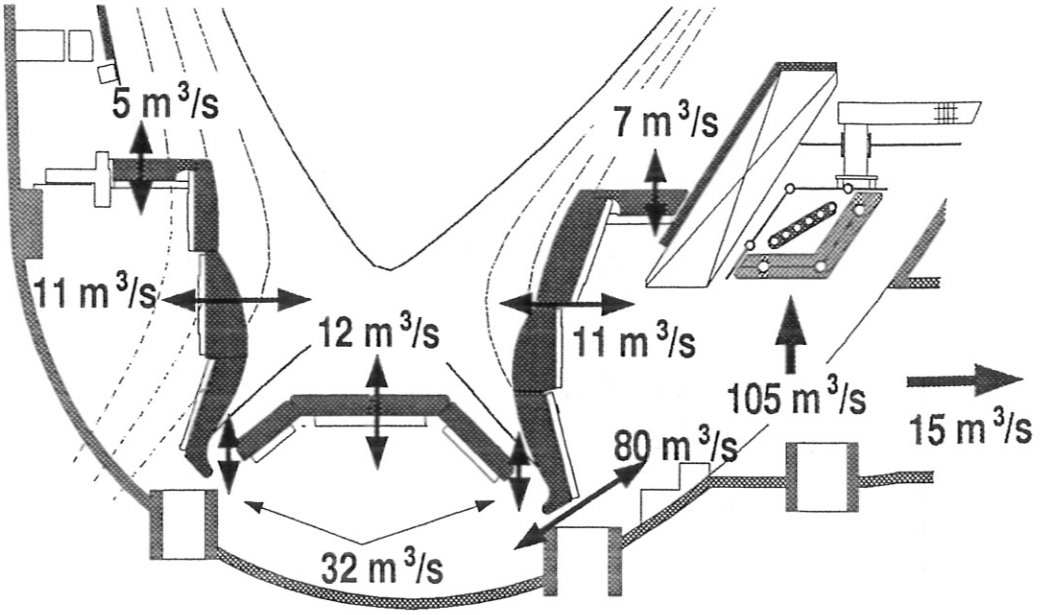

Figure 3

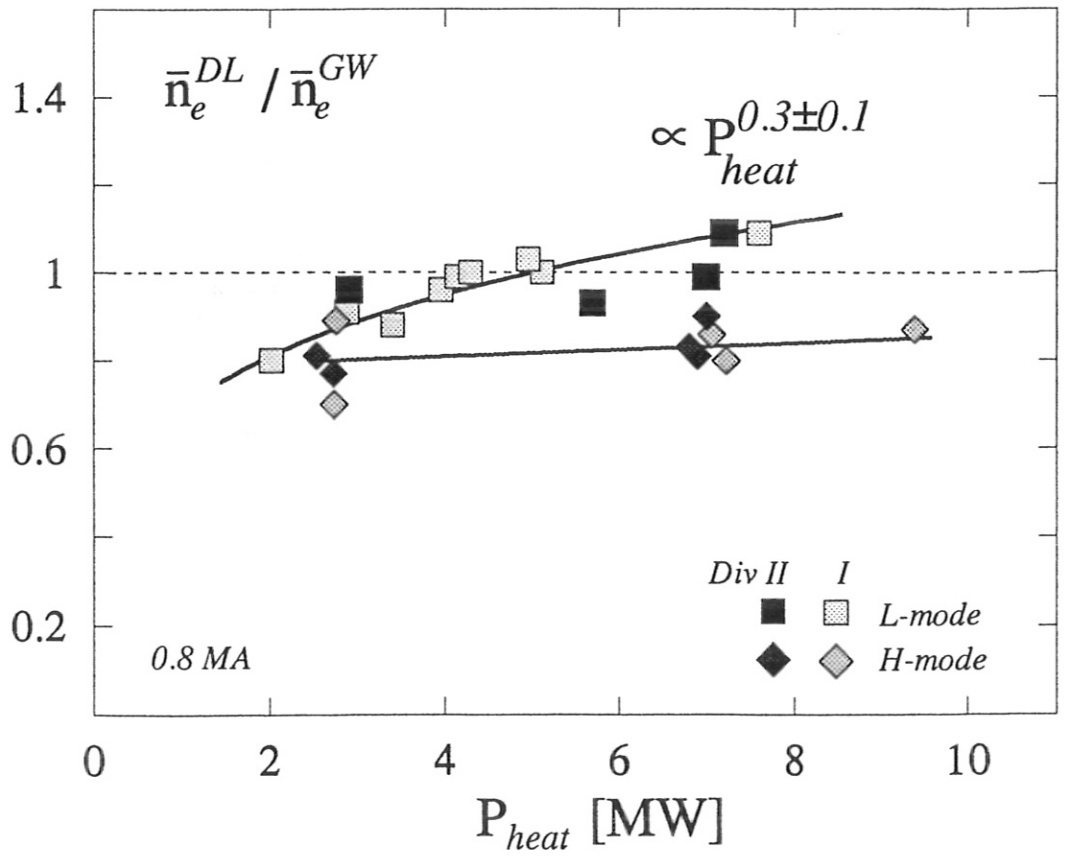

Figure 4

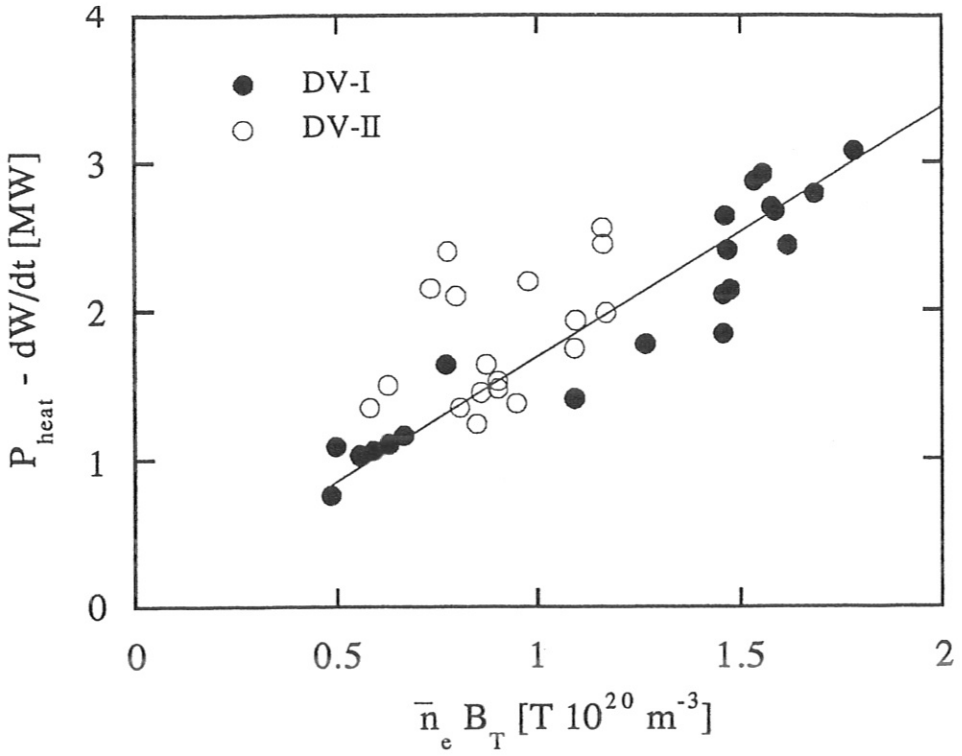

Figure 5

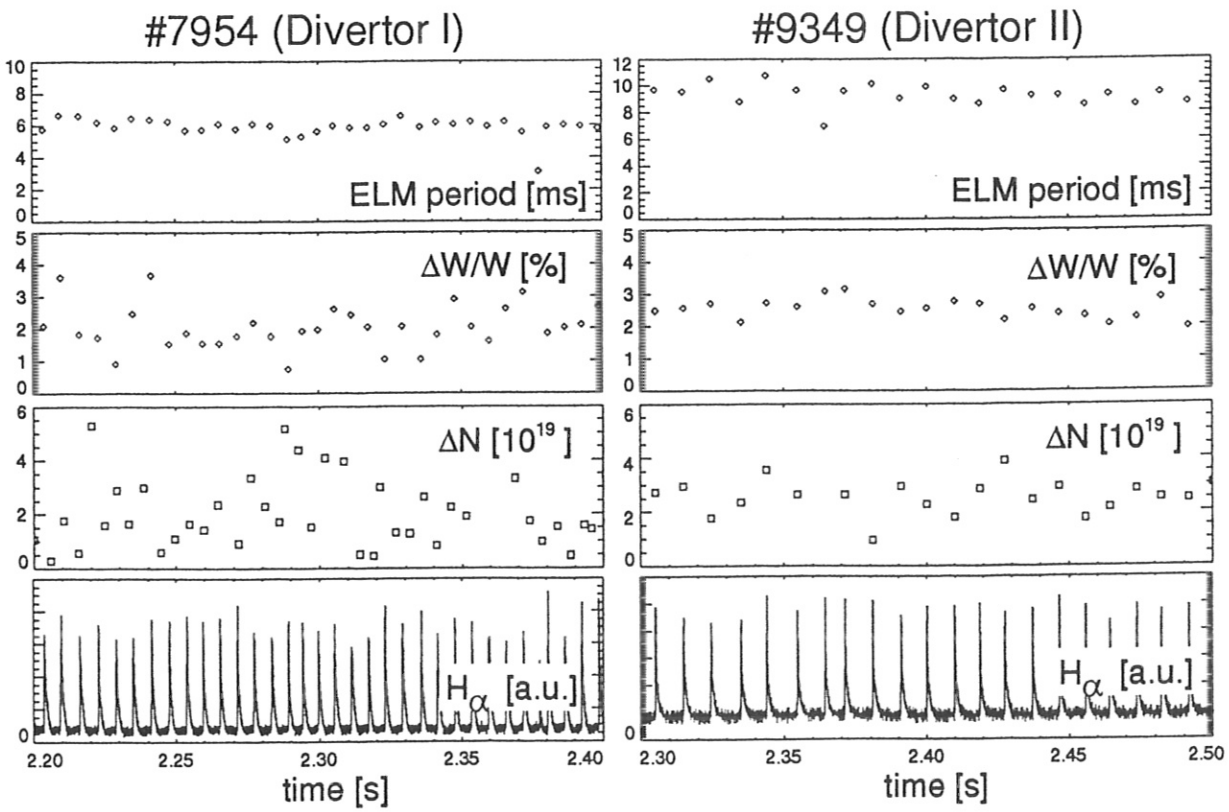

Figure 6

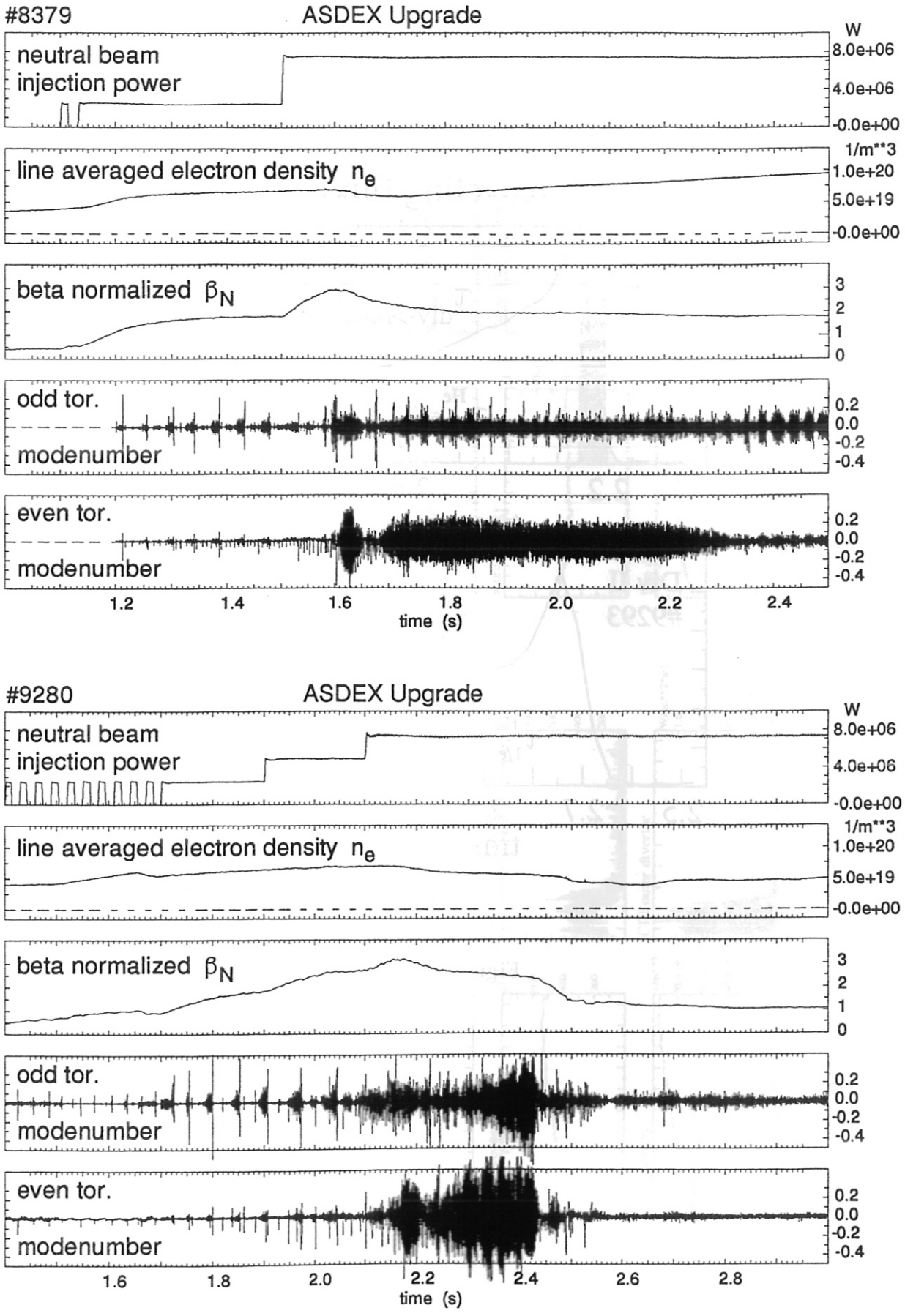
#8379
ASDEX Upgrade
neutral beam
injection power
W
8.0e+06
4.0e+06
-0.0e+00
line averaged electron density n_e
1/m**3
1.0e+20
5.0e+19
-0.0e+00
beta normalized β_N
3
2
1
0
odd tor.
modenumber
0.2
0.0
-0.2
-0.4
even tor.
modenumber
0.2
0.0
-0.2
-0.4
1.2
1.4
1.6
1.8
2.0
2.2
2.4
time (s)
#9280
ASDEX Upgrade
neutral beam
injection power
W
8.0e+06
4.0e+06
-0.0e+00
line averaged electron density n_e
1/m**3
1.0e+20
5.0e+19
-0.0e+00
beta normalized β_N
3
2
1
0
odd tor.
modenumber
0.2
0.0
-0.2
-0.4
even tor.
modenumber
0.2
0.0
-0.2
-0.4
1.6
1.8
2.0
2.2
2.4
2.6
2.8
time (s)

Figure 7

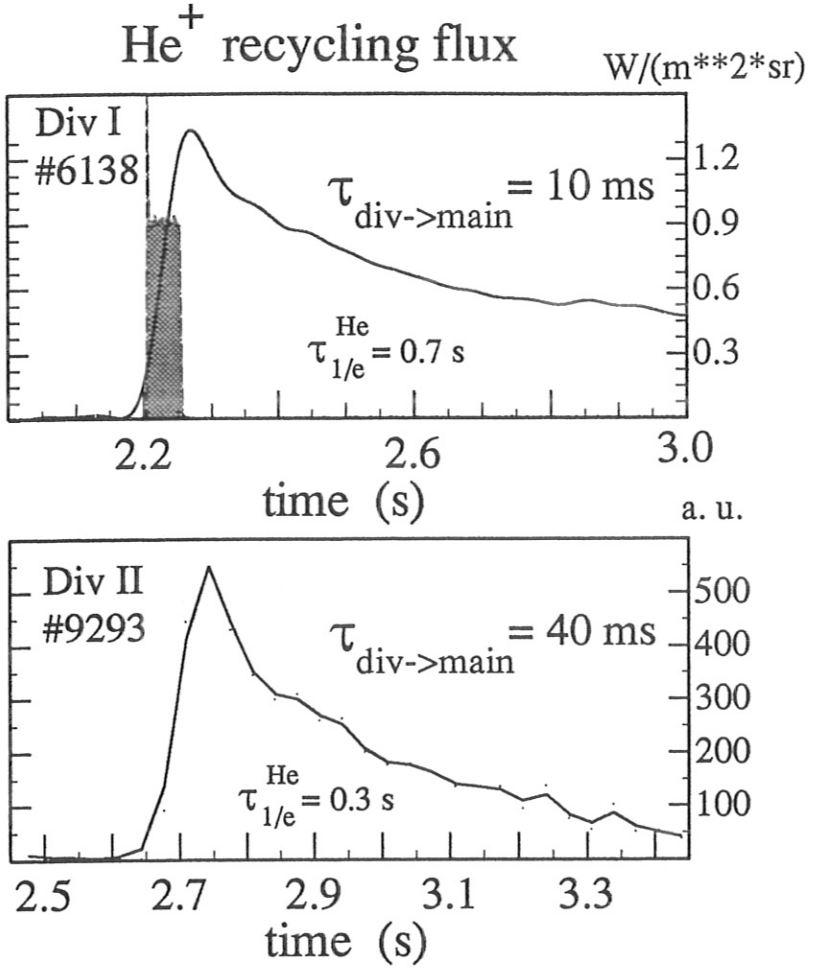
He+ recycling flux
W/(m**2*sr)
Div I
#6138
τ div->main = 10 ms
τ He 1/e = 0.7 s
1.2
0.9
0.6
0.3
2.2
2.6
3.0
time (s)
a. u.
Div II
#9293
τ div->main = 40 ms
τ He 1/e = 0.3 s
500
400
300
200
100
2.5
2.7
2.9
3.1
3.3
time (s)

Figure 8

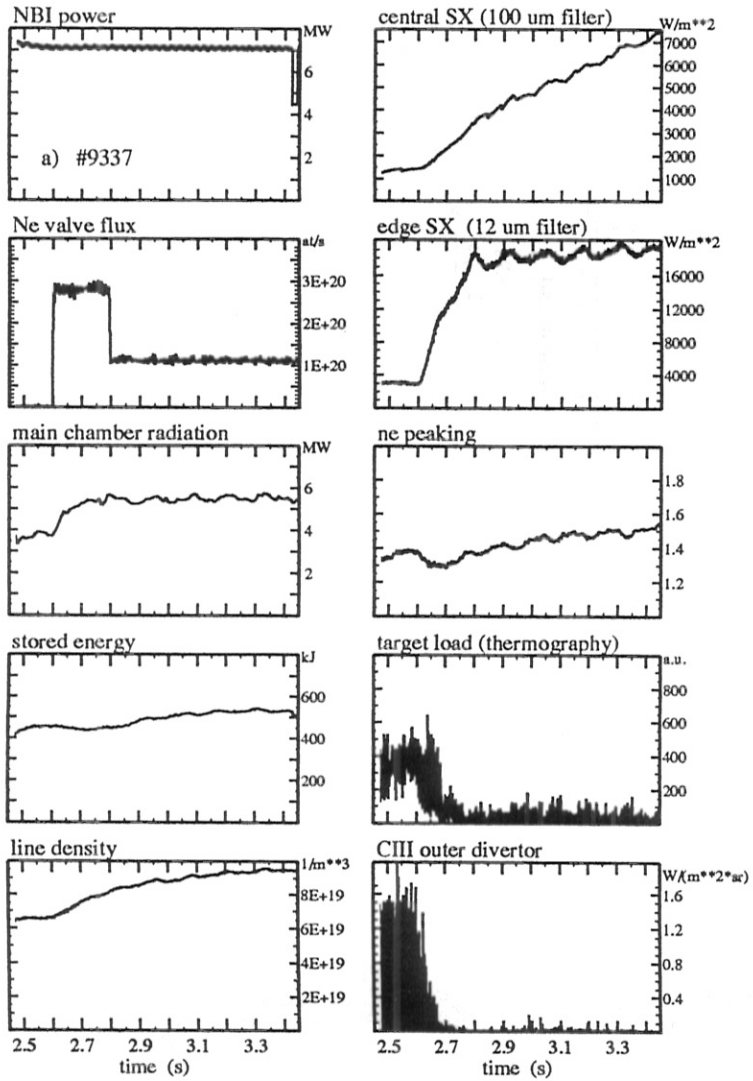

Figure 9a

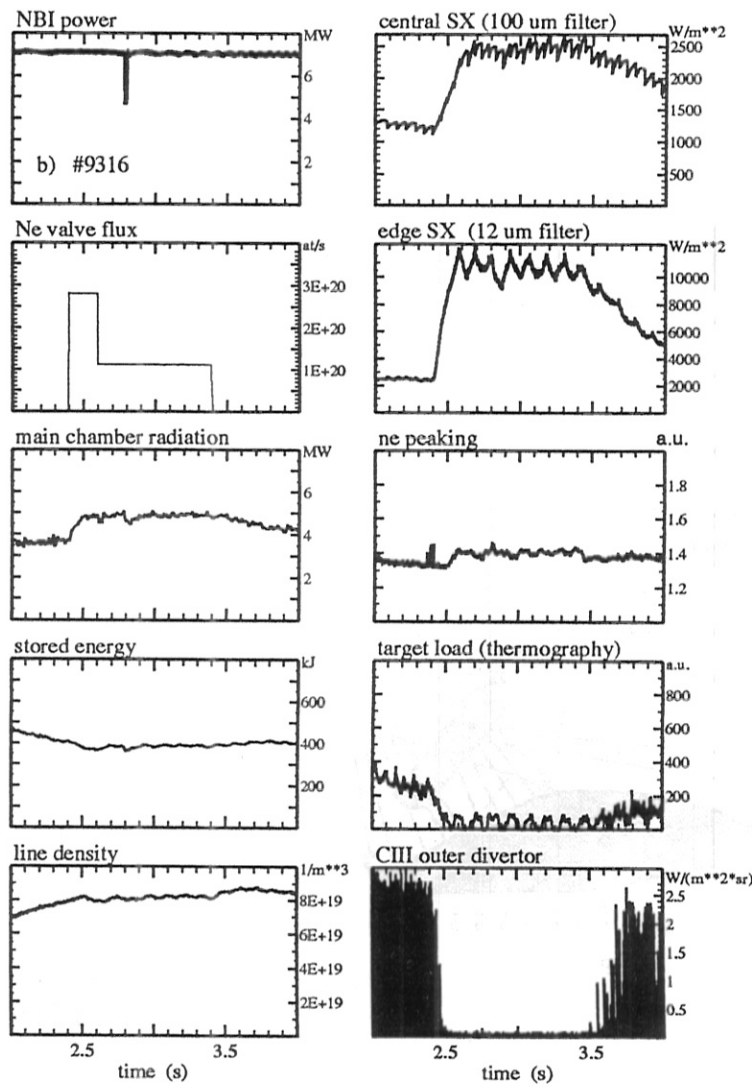

Figure 9b

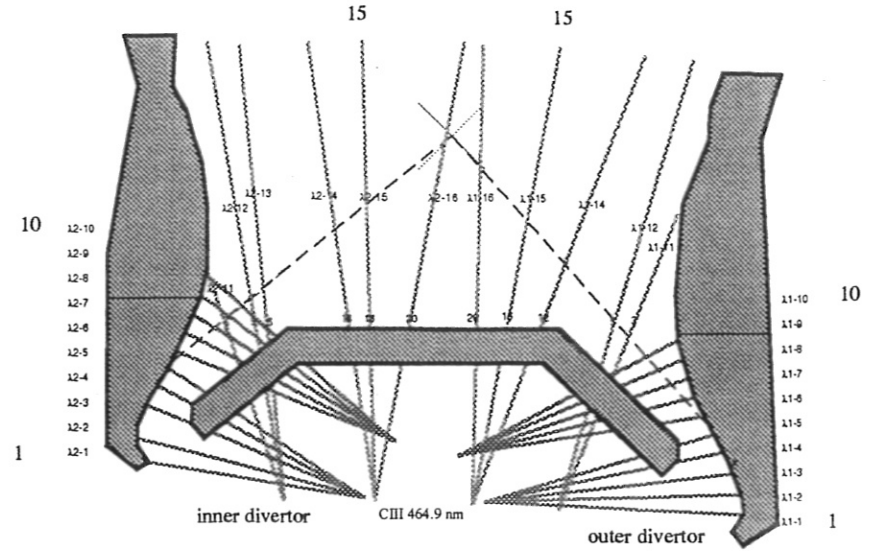
15
15
10
10
1
1
inner divertor
CIII 464.9 nm
outer divertor

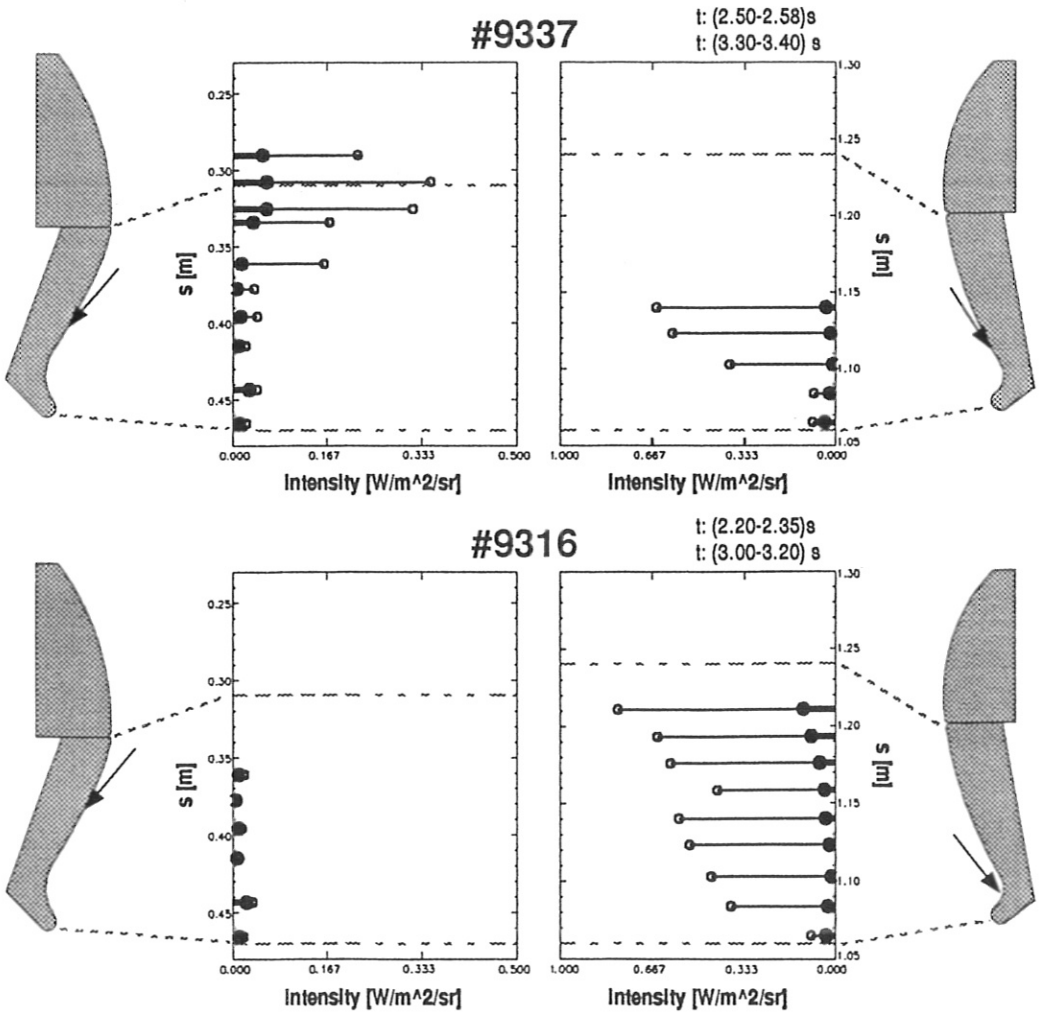
#9337
t: (2.50-2.58)s
t: (3.30-3.40) s
s [m]
Intensity [W/m^2/sr]
#9316
t: (2.20-2.35)s
t: (3.00-3.20) s
s [m]
Intensity [W/m^2/sr]

Figure 10